Ground Motion Model Incorporating Azimuthal Dependence on Topographic Effects in Japan

Authors

Jangsoo Lee[a], Junyoung Lee[a], and Byungmin Kim[a*]

Affiliation

[a] Dept. of Civil, Urban, Earth, and Environmental Engineering, Ulsan National Institute of Science and Technology, 50, UNIST-gil, Eonyang-eup, Ulju-gun, Ulsan 44919, Republic of Korea.

Correspondence

[*]Corresponding author. E-mail: byungmin.kim@unist.ac.kr

Ground Motion Model Incorporating Azimuthal Dependence on Topographic Effects in Japan

Jangsoo Lee[a], Junyoung Lee[a], and Byungmin Kim[a*]

[a] Dept. of Civil, Urban, Earth, and Environmental Engineering, Ulsan National Institute of Science and Technology, 50, UNIST-gil, Eonyang-eup, Ulju-gun, Ulsan 44919, Republic of Korea.

[*]Corresponding author. E-mail: byungmin.kim@unist.ac.kr

ABSTRACT

Conventional topographic terms in ground motion models (GMMs) typically characterize topographic effects using site-specific parameters such as relative elevation, curvature, or slope. This study demonstrates that topographic response is influenced by source-to-site geometry, specifically the incidence direction with respect to the slope aspect. Utilizing 15,189 records from 641 Kiban–Kyoshin network (KiK-net) stations in Japan, we analyze the corrected within-event residuals from which path, source, and site effects are eliminated. We introduce the azimuthal difference (α) between slope aspect and epicentral direction alongside the relative elevation (h_r) to capture the directional influences of incoming seismic waves on topographic response. Our empirical findings reveal that topographic effects (amplification or deamplification) are determined by the interplay between h_r and α, where facing slopes ($\alpha = 0°$) at ridges exhibit maximum amplification, while back slopes ($\alpha = 180°$) can induce deamplification. These responses exhibit a period-dependence, appearing prominently at short-to-intermediate periods ($T \leq 0.3$ s) where the seismic wavelength is comparable to the topographic scale, but diminishing at longer periods as the wavelength exceeds the topographic scale. By parameterizing this azimuthal dependence into a topographic term (f_{topo}), the model effectively reduces the standard deviation of the residuals.

1. INTRODUCTION

Topographic effects refer to the amplification or deamplification of ground motions due to the geometric characteristics of irregular terrain. It is particularly well known that ground motions are predominantly amplified at sites located on convex terrains, such as ridges, crests, and hills, relative to the surrounding area. These effects have been empirically documented over several decades through numerous field observations. Early instrumental evidence was captured during the 1971 San Fernando earthquake and its subsequent aftershocks, where pronounced amplification was recorded at the Pacoima Dam and several Californian mountain crests (Davis & West, 1973; Perez, 1973). Similar observations were subsequently reported worldwide, including Osakayama Hill in Japan (Nishimura & Morii, 1984), Canal Beagle in Chile (Çelebi, 1987), and Robinwood Ridge in California (Hartzell *et al.*, 1994). More catastrophic evidence emerged from the 1994 Northridge earthquake, where extreme topographic amplification contributed to severe structural failure at the Tarzana station in California, USA (Spudich *et al.*, 1996), and more recently, at the IBRH11 station in Japan during the 2011 Tohoku earthquake (Satoh *et al.*, 2014). Contemporary studies continue to report such topographic effects across diverse regions and geometries, including Tarzana Hill in California, USA (Graizer, 2009); Little Red Hill in New Zealand (Buech *et al.*, 2010); Narni Village in Italy (Massa *et al.*, 2010); Mt. Dong in China (Luo *et al.*, 2020); Gokgang-ri in South Korea (Kang *et al.*, 2019); and embankments of reservoirs in South Korea (Lee *et al.*, 2025).

Beyond empirical observations, numerical simulations have been extensively employed to identify the controlling parameters of topographic amplification. Bouchon and Barker (1996) examined the topographic amplification in the frequency range from 2 to 15 Hz at Tarzana hill in California, USA. Paolucci (2002) compared two-dimensional (2D) and three-dimensional (3D) topographic effects at various sites in Italy. Assimaki *et al.* (2005) parameterized various factors such as the dominant frequency of input motion, the bedrock-soil impedance ratio, the depth-to-bedrock ratio, and the relative thickness and flexibility of a surface layer to explain topographic effects in Athens, Greece. Lee *et al.* (2009) investigated peak ground acceleration (PGA) amplification considering variations in source frequency, source depth, wave-field type, and subsurface models in the Yangminshan region of Taiwan. Assimaki and Jeong (2013) conducted a parametric study on surface soil stiffness, soil thickness, and soil–bedrock impedance, inspired by the observations from the 2010 Haiti earthquake. Maufroy *et al.* (2015) introduced parameters such as the curvature smoothing range and the S-wave wavelength to evaluate topographic effects. Mohammadi and Asimaki (2017) analyzed the soil–topography coupling effects by parameterizing slope height, slope depth, thickness of surface layer, and shear wave velocity. Luo et al. (2020) evaluated the influence of stratigraphy and topography by modeling 2D and 3D representations of Mt. Dong in China with various subsurface structures. Li *et al.* (2022) investigated topographic amplification on slopes by considering soil type, slope height, slope angle, and the peak acceleration of input motion. Fang *et al.* (2023) examined the influence of soil property on topographic effects. Furthermore, several studies have proposed predictive models for topographic effects based on surface geometry parameters such as the relative elevation (h_r), curvature, and slope angle (Kim *et al.*, 2024; Park *et al.*, 2022; Rai *et al.*, 2017; Rai *et al.*, 2016). While these frameworks have demonstrated a significant correlation between site-specific parameters and topographic effects, they have primarily treated these responses as site-specific stationary properties, overlooking the azimuthal interaction between the incoming wavefield and terrain geometry. Consequently, there remains a lack of empirical evaluations that incorporate the seismic incidence direction as a predictive variable alongside conventional site-specific parameters.

This azimuthal dependence originates from the complex interaction between the incident wavefield and the three-dimensional terrain geometry, where the ground motion is significantly modulated by the slope orientation relative to the source. The seismic wavefield can be altered depending on whether the slope aspect is oriented toward or away from the source. This directional effect is empirically supported by observations from the 2017 Pohang earthquake, where Kang et al. (2019) reported that structures located on slopes facing the epicenter sustained severe damage compared to those on the back slopes. Based on these observations, Lee *et al.* (2026) demonstrated that ground motion amplification is modulated by the combined effects of relative elevation (h_r) and the azimuthal difference between slope aspect and epicentral direction (α), using localized data from Pohang, South Korea. Their results showed that for $\alpha < 90°$ (i.e., the slope facing the epicenter) ground motions were deamplified when $h_r < -18$ m and amplified when $h_r > 14$ m. In contrast, for $\alpha > 90°$ (i.e., the slope facing away from the epicenter) ground motions were deamplified when $h_r > 14$ m. However, their findings remain constrained to small-scale topographic environments, localized micro-earthquakes (i.e., local magnitude ranging from −1.1 to 1.7), with pronounced effects observed only in the short-period range of 0.01–0.1 s, leaving the generalizability of this directional effect unresolved. This direction-dependent topographic behavior has not yet been sufficiently incorporated into existing GMMs, due to the scarcity of empirical quantifications across diverse topographic scales and periods.

Motivated by the need to examine the generality of the azimuth-dependent topographic effects reported by Lee et al. (2026), this study investigates the variability of ground motion response throughout Japan. Unlike that study, which was limited to a localized topographic environment and a relatively small topographic scale, this study considers diverse and large-scale topographic configurations and evaluates the azimuth-dependent topographic effects by jointly considering h_r and α. To evaluate these topographic effects in Japan, we utilize the Kiban-Kyoshin Network (KiK-net) dataset compiled by Dawood *et al.* (2016), which provides a comprehensive collection of seismic metadata and spectral accelerations across a range of periods. To systematically isolate topographic effects, we first account for the source and path effects by employing the reference GMM derived by Kotha *et al.* (2018), which incorporates moment magnitude (**M**) and the Joyner–Boore distance (R_{JB}). Subsequently, we partition the residuals into between-event and within-event residuals and eliminate the site effect governed by the time-averaged shear wave velocity in the upper 30 m (V_{S30}) from the within-event residuals. The remaining residuals are analyzed with respect to topographic parameters (h_r and α). These parameters were derived from a Digital Elevation Model (DEM) using ArcGIS, as described in the section “Topographic parameters”. Finally, we develop a comprehensive GMM that incorporates a novel topographic term dependent on both h_r and α, alongside path, source, and site effects.

2. DATA

2.1. Ground motions in Japan

Dawood et al. (2016) compiled a comprehensive dataset that includes earthquake magnitude and location, station location, V_{S30}, source-to-station distance, and pseudo spectral acceleration (PSA) at various periods (i.e., T = 0.01–10 s), etc. The data selection process followed the five criteria outlined by Kotha et al. (2018) to ensure the inclusion of high-quality records: 1) Category A, representing the strictest error margin; 2) Active Shallow Crustal events (ACRsh); 3) focal depth $\leq$ 35 km; 4) surface recordings with measured V_{S30} available; and 5) all six-component (two horizontal and one vertical components at both borehole and surface) of ground motions with signal-to-noise ratio (SNR) $\geq$ 3 within a frequency bandwidth range from high-pass corner frequency (f_c) to 30 Hz. The initial dataset of approximately 157,000 records was reduced to 15,189 records through the data selection process. The final dataset utilized in this study is illustrated in Figure 1, which shows the locations of 641 stations and the magnitudes and epicenters of 838 events. As summarized in Figure 2(a–d), the selected

15,189 records span R_{JB} values from 0 to 600 km. The 838 events have focal depth ranging from 5 to 35 km and **M** ranging from 3.4 to 6.9. The stations have V_{S30} values ranging from 106 to 2,100 m/s.

2.2. Topographic parameters

We utilized a Digital Elevation Model (DEM) with a 1 arc-second (~30 m) spatial resolution from the Shuttle Radar Topography Mission (SRTM), provided by the United States Geological Survey (USGS). Two primary topographic parameters were derived using ArcGIS: relative elevation (h_r) and azimuthal difference between slope aspect and epicentral direction (α).

h_r quantitatively indicates the difference between the elevation of a station and its surrounding mean elevation (h_{mean}). To account for the multiscale nature of topography, h_r was calculated using different search radii. For a given radius, h_r^{radius} is defined as the difference between the station elevation (h) and the mean elevation within that radius (h_{mean}^{radius}) in meters:

$$h_r^{radius} = h - h_{mean}^{radius} \tag{1}$$

A positive h_r indicates convex regions such as ridges, whereas a negative h_r indicates concave regions such as valleys. Figure 3(a and b) shows a satellite image and elevation map of Japan, respectively. Figure 3(c and d) shows an example of a mean elevation within a radius of 1,000 m (h_{mean}^{1000}) and a relative elevation at a 1,000 m-scale (h_r^{1000}), respectively.

To account for the azimuthal dependence of the topographic effects, we introduced α, which represents the angular difference between the azimuth of the slope aspect (ϕ_{slope}) and the station-to-source azimuth (ϕ_{epi}). Both azimuths are measured in degrees clockwise from North. Specifically, α was constrained to range from 0° to 180°, where $\alpha = 0°$ indicates that the slope faces toward the epicenter (facing slope), whereas $\alpha = 180°$ indicates that the slope faces away from the epicenter (back slope). Furthermore, to reflect the topographic scale of the terrain geometry, we computed the smoothed α (α^{radius}) using the ϕ_{slope} derived from the mean elevation for a specified radius (ϕ_{slope}^{radius}) as follows:

$$\alpha^{radius} = \begin{cases} \left|\phi_{slope}^{radius} - \phi_{epi}\right| & \text{if } \left|\phi_{slope}^{radius} - \phi_{epi}\right| \le 180° \\ 360° - \left|\phi_{slope}^{radius} - \phi_{epi}\right| & \text{if } \left|\phi_{slope}^{radius} - \phi_{epi}\right| > 180° \end{cases} \tag{2}$$

Here, α for ϕ_{slope} derived from the native-resolution DEM is denoted as α^{DEM}. Figure 3(e and f) shows examples of the native-scale ϕ_{slope} and α^{DEM}.

The distributions of the topographic parameters are shown in Figure 2. Figure 2(e) shows that most of the 641 KiK-net stations are concentrated at relatively low elevations, particularly below approximately 300 m. Similarly, the distribution of h_r^{1000}, as shown in Figure 2(f), is concentrated near zero with a slight tendency toward negative, showing that most sites are not on hilltops or ridges. Figure 2(g and h) illustrates the distributions of ϕ_{epi} and ϕ_{slope}. The distribution of α at a 100 m-scale (α^{100}), derived from both ϕ_{slope}^{100} and ϕ_{epi}, is shown in Figure 2(i). In the subsequent section, we employed h_r^{radius} and α^{radius} as topographic parameters to develop a topographic term.

3. RESIDUAL DECOMPOSITION USING A MIXED-EFFECTS MODEL

3.1. Source and path effects

To quantify topographic response from the ground motions, we developed a base GMM by performing a regression analysis. We adopted the functional forms for source and path effects proposed by Kotha et al. (2018) (hereafter Ko18). The analysis was conducted using pseudo-spectral acceleration (PSA) at 12 periods (i.e., T = 0.01, 0.02, 0.03, 0.05, 0.075, 0.1, 0.2, 0.3, 0.5, 0.75, 1 and 2 s), calculated as the geometric mean of two horizontal components. (i.e., East-West (EW) and North-South (NS) components). The numbers of records available for analysis were 15,189 for periods of 0.01–0.5 s, 13,802 for periods of 0.75–1 s, and 6,646 for a period of 2 s, because the maximum usable period for each record was defined as $T_{max} = 0.5/f_c$ (Dawood et al., 2016). Although the initial dataset included response spectra up to 10 s, only periods of $T \leq 2$ s were considered in this study due to the data sparsity at longer periods. The form of Ko18 that incorporates a mixed-effects model is conceptualized as follows:

$$\ln(\mathrm{PSA}) = f_{\mathrm{R}}(\mathbf{M}, R_{JB}) + f_{\mathrm{M}}(\mathbf{M}) + \delta B_e + \delta W_{es} \quad (3)$$

where PSA is 5% damped pseudo spectral acceleration at a period, **M** is moment magnitude, R_{JB} is the Joyner–Boore distance, f_{R} and f_{M} are the distance and magnitude scaling terms, δB_e is the between-event residuals for e^{th} event, and δW_{es} is the within-event residuals for e^{th} event at s^{th} site. The specific functional forms for f_{R} and f_{M} adapted from Ko18 are described in APPENDIX.

3.2. Site-effect correction

Following the framework of Ko18, we first calculated the total residuals by removing the source and path effects utilizing f_R and f_M. These total residuals were subsequently partitioned into between-event and within-event components. As illustrated in Figure A1, the between-event residuals exhibit no systematic trends with respect to **M**, and the within-event residuals show no systematic dependence on R_{JB}.

Using the within-event residuals, we accounted for site effects by evaluating the V_{S30}-dependent trends. The V_{S30}-correction process was conducted in two sequential stages to ensure that the site-specific effect was captured across the 12 spectral periods.

In the first stage, for each period, we computed the site-averaged within-event residuals for each station. This average represents the systematic bias of a particular site at a given period. We then modeled the relationship between these station-averaged residuals and V_{S30} using the LOESS (Locally Weighted Regression and Smoothing Scatterplots) function (Cleveland, 1979), as illustrated in Figure A2. The site term modeled by the LOESS fit, denoted as $f_{\text{site}}(V_{S30})$, captures the systematic site response associated with V_{S30} for each period.

In the second stage, we derived the V_{S30}-corrected within-event residual ($\delta W_{es}{}^{*}$) by subtracting the corresponding V_{S30}-dependent site term (f_{site}) value from the within-event residuals as follows:

$$\delta W_{es}{}^{*} = \delta W_{es} - f_{\text{site}}(V_{S30}) \quad (4)$$

where δW_{es} represents the within-event residual for e^{th} event at s^{th} site. These corrected residuals, $\delta W_{es}{}^{*}$, from which the dominant V_{S30} influence has been eliminated, are used to quantify topographic responses in the subsequent section.

4. CHARACTERIZATION OF AZIMUTH-DEPENDENT TOPOGRAPHIC EFFECTS

4.1. Azimuth-dependent topographic response

We evaluated the remaining variability (i.e., $\delta W_{es}{}^{*}$) using two key topographic parameters, h_r^{radius} and α^{radius}, across a range of radius scales. To identify the optimal topographic scale that best captures the topographic response, we calculated h_r for scale radius ranging from 100 to 3,000 m, while α for native resolution (i.e., α^{DEM}) and scale radius of 50 and 100 m. We then classified the ground motion data into high- and low-relative elevation groups based on the upper and lower 1% of h_r^{radius}, respectively. This threshold was selected to isolate sites with the strongest relative topographic contrast, corresponding to pronounced ridge-like and valley-like geometries where topographic effects are expected to be most clearly observed.

Conventional GMMs typically employed h_r as a sole parameter to account for topographic effect, assuming a monotonic amplification occurs at ridges characterized by high h_r values. In contrast, valley sites characterized by low h_r values experiences deamplification. However, our empirical findings show that the ground motion response is significantly modulated by the incidence direction with respect to the slope aspect, consistent with the findings of Lee et al. (2026). Figure 4 conceptually depicts 4 representative cases characterized by h_r (high versus low) and α (0° versus 180°) under oblique incidence. At the ridge facing toward the epicenter ($h_r > 0$, $\alpha = 0°$), the incident seismic wave propagates along the slope surface, facilitating the generation of surface waves that maximize seismic amplification. Conversely, at the ridge facing away from the epicenter ($h_r > 0$, $\alpha = 180°$), the incident seismic wave experiences attenuation due to its longer path compared to the ridge facing toward the epicenter. At the valley facing toward the epicenter ($h_r < 0$, $\alpha = 0°$), the terrain geometry causes scattering and energy dispersion due to its convexity, leading to seismic deamplification. These inferences are consistent with the empirical trends observed in the actual seismic dataset and underscore the necessity of incorporating azimuthal parameters into the topographic term of GMMs.

We evaluated h_r scales ranging from 100 to 3000 m and α scales from the DEM resolution to 100 m. For clarity, Figure 5 illustrates δW_{es}^{*} versus α^{100} for the high- and low-h_r groups defined using h_r^{500}, h_r^{1000}, and h_r^{1500} at T = 0.02, 0.2, and 2 s. These scales were selected to illustrate how the azimuth-dependent topographic response varies with the spatial scale of relative elevation. For h_r^{1000}, 151 out of 15,189 ground motions were categorized into high-h_r ($h_r^{1000} > 45$ m), whereas 161 out of 15,189 ground motions were categorized into low-h_r elevation ($h_r^{1000} < -150$ m), for T = 0.02 and 0.2 s, as illustrated in Figure 5(b and e). For T = 2 s, 59 and 46 out of 6,646 records were classified into high and low h_r^{1000} groups, respectively (Figure 5(h)). The same method for classification of high- and low-h_r groups was applied to other scales of h_r^{radius}. In contrast, the intermediate-h_r groups exhibited no discernible trend with respect to α^{radius}, as shown in Figure A3 and were consequently excluded from the topographic correction model.

Among the combinations of various scales of h_r^{radius} and α^{radius}, pronounced trends of topographic effect were primarily observed for h_r^{radius} scales of 1,000 m or larger and α^{radius} scales 50 m or larger for $T \leq 0.3$. Specifically, as shown in Figure 5(b and e), the high h_r groups defined by h_r^{1000} show the mean residuals of 0.49 and 0.57 at $\alpha^{100} = 9°$ for T = 0.02 and 0.2 s, respectively. These values gradually decrease to –0.33 and –0.24 as α^{100} increases to 171°. This indicates that seismic amplification at ridge is maximized when the slope aspect is oriented toward the epicenter (i.e., facing slope) whereas deamplification occurs as the slope faces away from the epicenter (i.e., back slope). Conversely, for T = 0.02 and 0.2 s, the low h_r groups defined by h_r^{1000} show that the mean residual of –0.47 and –0.44 at $\alpha^{100} = 9°$, respectively. These values increase to approximately 0 near $\alpha^{100} = 90°$ and remain close to zero thereafter. This indicates that deamplification at low relative elevation is dominant for facing slopes. The same azimuth-dependent trends for both high- and low-h_r groups were observed at the h_r^{1500} scale. This behavior aligns with the findings of Lee et al. (2026) in Pohang, South Korea, where a similar azimuth-dependence was reported using a localized seismic network. However, while their topographic term was optimized for the h_r^{300}scale due to the smaller topographic scale of that region, the azimuth-dependent topographic effects in our empirical observations are identified for the h_r^{1000} scale, reflecting the larger topographic scale of Japan.

Figure 5(a and d) shows a substantially weaker azimuth-dependent trend for h_r^{500}. This scale-dependence implies that for the present dataset, the azimuthal modulation of ground motion is more evident when larger-scale topographic features are considered. The selection process of optimal spatial resolution for topographic parameters is described in the subsequent section.

For both high- and low-h_r, the azimuthal dependence of topographic effects is distinct at short-to-intermediate periods, particularly at T = 0.02 and 0.2 s. In contrast, the azimuthal dependence diminishes significantly at T = 2 s, as illustrated in Figure 5(h and i). Similar behavior is observed across other scale combinations, where azimuth-dependent topographic effects are evident primarily for h_r^{radius} scales equal to or greater than 1,000 m and α^{radius} scales greater than 50 m. Together, these observations indicate that the topographic effects are period-dependent. The significant trends at short-to-intermediate periods ($T \leq 0.3$ s) suggest a loss of sensitivity to terrain geometry in the long-period range. This period-dependency is governed by the physical relationship between the seismic wavelength and the characteristic scale of the terrain. When the wavelength of long-period waves significantly exceeds the topographic scale, the influence of local topographic irregularities on wave propagation becomes progressively weaker, and scattering and interference effects become less pronounced. Consequently, the azimuthal orientation of the slope becomes irrelevant to the ground motion amplification or deamplification.

4.2. Development of a topographic term

Based on empirical observations in the previous section, we developed the topographic correction term at periods ranging from 0.01 to 2 s. We proposed the linear relationship between the V_{S30}-corrected within-event residuals (δW_{es}^{*}) and the aspect-to-source azimuthal difference (α) in case of high- and low-h_r groups, respectively. The thresholds for each case of high- and low-h_r were set to divide the upper and lower 1% h_r.

Equation (5) shows the proposed functional form developed separately for each high-and low-h_r^{1000} cases.

$$f_{\text{topo}}(h_r^{1000}, \alpha^{100}) = \begin{cases} e_1 + e_2 \times \alpha^{100} & \text{for } h_r^{1000} > 45\text{ m} \\ e_3 + e_4 \times \alpha^{100} & \text{for } h_r^{1000} < -150\text{ m} \end{cases} \tag{5}$$

e_1, e_2, e_3, and e_4 represent the period-dependent regression coefficients, summarized in Table 1. Examples of the proposed model at periods of 0.02 ,0.2, and 2 s are shown as the regression lines in Figure 5(b, e, and h), respectively.

To determine the optimal spatial resolution for the topographic parameters, we examined the standard deviation (SD) after the topographic correction in all combinations of h_r^{radius} and α^{radius} for each period. Since the azimuth dependence on topographic effects was observed at short-to-intermediate periods ($T \leq 0.3$ s), our evaluation focused on the residual SD after the topographic correction within this range. The combination of h_r^{1000} and α^{100} yielded the lowest residual SD at T = 0.01–0.1 s, as summarized in Table 2. This suggests that h_r^{1000} and α^{100} is the optimal scale for describing the azimuth-dependent topographic effects. Therefore, we adopted h_r^{1000} and α^{100} as the topographic parameters to construct the azimuth-dependent topographic term. As illustrated in Figure 6, the topography-corrected residuals ($\delta W_{es}^{*} - f_{\text{topo}}(h_r^{1000}, \alpha^{100})$) demonstrate a significant reduction in the systematic azimuthal trends previously observed. This reduction in uncertainty indicates that incorporating α effectively accounts for systematic topographic effects that were previously unmodeled in the topographic term of existing GMMs.

Lee et al. (2026) proposed topographic term (f_{topo}) coefficients considering both h_r and α^{DEM} at short-to-intermediate periods ($T \leq 0.5$ s) through a linear function formulated for high- and low-h_r groups, using α derived from a DEM with 30 m resolution. For high-h_r groups, the slope coefficients for f_{topo} are -7.68×10^{-3} and 4.50×10^{-4} at T = 0.02 and 0.2 s, respectively (Lee et al., 2026). Comparing these values with the results of this study indicates that both studies exhibit highly consistent azimuthal dependencies at T = 0.02 s. Specifically, the same physical trend is observed where ground motions amplify on slopes facing toward the epicenter and deamplify on slopes facing away. However, the azimuthal effect becomes significantly more pronounced in Japan at T = 0.2 s, which means that azimuth-dependent topographic effects extend into the longer period. This phenomenon occurs because larger terrain geometries interact more strongly with longer seismic wavelengths, which physically justifies our adoption of broader topographic scales (h_r^{1000} and α^{100}) than those used by Lee et al. (2026). For low-h_r groups, the slope coefficients from Lee et al. (2026) are 8.20×10^{-3} and 6.49×10^{-3} at T = 0.02 and 0.2 s, respectively, showing that a consistent azimuth-dependent mechanism is verified for valley-like sites as well. Specifically, both studies confirm that deamplification in valleys remains dominant for facing slopes and systematically diminishes for the back slopes.

As shown in Figure 7, we compared the GMM from the base model ($f_R + f_M$) with those from the proposed GMM incorporating the azimuth-dependent topographic term ($f_R + f_M + f_{topo}$). All predictions are conditioned on a fixed Magnitude (**M** 5.0) across α^{100} = 30°, 90°, and 150°. For α^{100} = 30°, the proposed GMM exhibited a 9–26% amplification in PSA for high-h_r group at T = 0.01–0.3 s where the topographic response is most pronounced. Conversely, for the low-h_r group at the same period range, the proposed GMM yields 5–31% deamplification. For α^{100} = 90°, no distinct amplification or deamplification was captured between the two GMMs. For α^{100} = 150° within the same period range, high-h_r group exhibits an 18–41% deamplification in PSA.

As shown in Figure 8, we also compared the base GMM with the proposed GMM across the entire evaluated period range (T = 0.01–2 s) under a fixed magnitude and source-to-site distance (**M** 4.0, R_{JB} = 150 km). For α^{100} = 30°, an amplification at short-to-intermediate periods (T = 0.01–0.3 s) was captured for high-h_r group however, this amplification diminished at longer periods (T > 0.3 s) as the predictions converge toward the baseline GMM. Conversely, a deamplification for low-h_r group was captured at the same period range, demonstrating that the azimuth-dependent topographic effects are confined to short-to-intermediate periods. For α^{100} = 90°, the proposed GMM yielded similar predictions to the base GMM across all periods for high- and low-h_r group. For α^{100} = 150°, a deamplification occurred for high-h_r group at T

= 0.01–0.3 s, which diminishes at T > 0.3 s.

5. CONCLUSIONS

This study investigated the azimuth-dependent topographic effects using 15,189 ground motion records from 641 KiK-net stations across Japan. By removing the source, path, and V_{S30} -dependent site effects using a reference GMM, the remaining residuals were analyzed with respect to topographic parameters. We identified the relative elevation scaled at a radius (h_r^{radius}) and the scaled azimuthal difference between slope aspect and epicentral direction (α^{radius}) as the topographic parameters.

Our findings demonstrate that topographic amplification is not a monotonic function of the relative elevation (h_r), as suggested by previous studies (e.g., Kim et al. (2024); Rai et al. (2016); Rai et al. (2017)), but is significantly modulated by the relative orientation between the slope aspect and the epicenter. At ridge-like sites (high-h_r), amplification is maximized for facing slopes ($\alpha = 0°$), whereas deamplification occurs for back slopes ($\alpha = 180°$). At valley-like sites (low-h_r), pronounced deamplification is observed for facing slopes. These results indicate that topographic effects depend on the incidence direction, even at the same site. Therefore, conventional topographic terms based solely on relative elevation are insufficient to fully describe topographic amplification patterns. The results highlight the necessity of jointly considering both h_r and α when parameterizing topographic effects in empirical GMMs.

The spatial scale of the topographic parameters also proved critical. In the study area, the most distinct ground motion responses were captured at h_r^{1000} and α^{100}. While we propose a topographic term based on these specific scales, it is important to note that the optimal scale and thresholds (e.g., h_r^{1000} > 45 m or < −155 m) are likely region-dependent and may vary with local terrain geometry. This scale dependence suggests that the characteristic dimensions of regional topography should be considered when defining topographic parameters for ground-motion prediction.

The consistent identification of azimuth-dependent topographic effects across different regions reinforces the reliability of this phenomenon. The empirical observation that ground motion amplification and deamplification are modulated by h_r and α directly aligns with independent regional studies in the literature (Lee et al., 2026). However, whereas Lee et al. (2026) demonstrated this behavior using a localized seismic network in Pohang, South Korea, the present study confirms that the same mechanism is observable across a nationwide dataset encompassing diverse topographic environments, a broader range of earthquake magnitudes, and a substantially larger number of earthquakes and recording stations. This consistency demonstrates that despite differences in regional topographic settings, earthquake magnitude ranges, and dataset sizes, the azimuthal dependence represents a fundamental and reproducible characteristic of topographic effects.

The observed topographic trends were prominent at short-to-intermediate periods ($T \leq 0.3$ s) but disappeared at longer periods. This suggests a period-dependent mechanism where the topography-azimuth dependence diminishes as the seismic wavelength exceeds the physical scale of the terrain geometry. By incorporating this azimuthal influence, the proposed model effectively reduces uncertainty, providing a more refined framework for regional seismic hazard assessments.

ACKNOWLEDGEMENTS

This study was supported by the Korea Meteorological Administration Research Development Program (KMI2022-00610) and the National Research Foundation of Korea (NRF) grant funded by the Korea government (MSIT) (RS-2026-25486755).

REFERENCES

Assimaki, D., Gazetas, G., & Kausel, E. (2005). Effects of Local Soil Conditions on the Topographic Aggravation of Seismic Motion: Parametric Investigation and Recorded Field Evidence from the 1999 Athens Earthquake. *Bulletin of the Seismological Society of America*, *95*(3), 1059-1089. https://doi.org/10.1785/0120040055

Assimaki, D., & Jeong, S. (2013). Ground-Motion Observations at Hotel Montana during the M 7.0 2010 Haiti Earthquake: Topography or Soil Amplification? *Bulletin of the Seismological Society of America*, *103*(5), 2577-2590. https://doi.org/10.1785/0120120242

Bouchon, M., & Barker, J. S. (1996). Seismic response of a hill: The example of Tarzana, California. *Bulletin of the Seismological Society of America*, *86*(1A), 66-72. https://doi.org/10.1785/bssa08601a0066

Buech, F., Davies, T. R., & Pettinga, J. R. (2010). The Little Red Hill Seismic Experimental Study: Topographic Effects on Ground Motion at a Bedrock-Dominated Mountain Edifice. *Bulletin of the Seismological Society of America*, *100*(5A), 2219-2229. https://doi.org/10.1785/0120090345

Çelebi, M. (1987). Topographical and geological amplifications determined from strong-motion and aftershock records of the 3 March 1985 Chile earthquake. *Bulletin of the Seismological Society of America*, *77*(4), 1147-1167. https://doi.org/10.1785/bssa0770041147

Cleveland, W. S. (1979). Robust Locally Weighted Regression and Smoothing Scatterplots. *Journal of the American Statistical Association*, *74*(368), 829-836. https://doi.org/10.1080/01621459.1979.10481038

Davis, L. L., & West, L. R. (1973). Observed effects of topography on ground motion. *Bulletin of the Seismological Society of America*, *63*(1), 283-298. https://doi.org/10.1785/bssa0630010283

Dawood, H. M., Rodriguez-Marek, A., Bayless, J., Goulet, C., & Thompson, E. (2016). A Flatfile for the KiK-net Database Processed Using an Automated Protocol. *Earthquake Spectra*, *32*(2), 1281-1302. https://doi.org/10.1193/071214eqs106

Fang, H., Wu, Y., Qu, C., & Lin, Y. (2023). Investigation of topographic amplification on ground motions considering spatial variability of soil properties. *Stochastic Environmental Research and Risk Assessment*, *38*(3), 901-922. https://doi.org/10.1007/s00477-023-02605-y

Graizer, V. (2009). Low-velocity zone and topography as a source of site amplification effect on Tarzana hill, California. *Soil Dynamics and Earthquake Engineering*, *29*(2), 324-332. https://doi.org/10.1016/j.soildyn.2008.03.005

Hartzell, S. H., Carver, D. L., & King, K. W. (1994). Initial investigation of site and topographic effects at Robinwood Ridge, California. *Bulletin of the Seismological Society of America*, *84*(5), 1336-1349. https://doi.org/10.1785/bssa0840051336

Kang, S., Kim, B., Cho, H., Lee, J., Kim, K., Bae, S., & Sun, C. G. (2019). Ground-Motion Amplifications in Small-Size Hills: Case Study of Gokgang-ri, South Korea, during the 2017 ML 5.4 Pohang Earthquake Sequence. *Bulletin of the Seismological Society of America*, *109*(6), 2626-2643. https://doi.org/10.1785/0120190064

Kim, B., Park, K., Baek, H., Lee, J., & Kweon, C. (2024). Models for topographic ground motion amplification based on finite element analyses considering topographic features and ground motions in Japan. *Natural Hazards*, *120*(13), 11825-11849. https://doi.org/10.1007/s11069-024-06662-6

Kotha, S. R., Cotton, F., & Bindi, D. (2018). A new approach to site classification: Mixed-effects Ground Motion Prediction Equation with spectral clustering of site amplification functions. *Soil Dynamics and Earthquake Engineering*, *110*, 318-329. https://doi.org/10.1016/j.soildyn.2018.01.051

Lee, J., Kim, K.-H., Kang, S. Y., & Kim, B. (2026). Ground-Motion Model Considering the Effects of Wave Propagation Direction and Topography in Pohang, South Korea. *Bulletin of the Seismological Society of America*. https://doi.org/10.1785/0120250295

Lee, J., Lim, S. K., & Kim, B. (2025). Ground Motion Amplifications at the Embankments of Reservoirs in South Korea. *Journal of Earthquake Engineering*, *29*(15), 3089-3107. https://doi.org/10.1080/13632469.2025.2558793

Lee, S. J., Chan, Y. C., Komatitsch, D., Huang, B. S., & Tromp, J. (2009). Effects of Realistic Surface Topography on Seismic Ground Motion in the Yangminshan Region of Taiwan Based Upon the Spectral-Element Method and LiDAR DTM. *Bulletin of the Seismological Society of America*, *99*(2A), 681-693. https://doi.org/10.1785/0120080264

Li, Y., Wang, G., & Wang, Y. (2022). Parametric investigation on the effect of sloping topography on horizontal and vertical ground motions. *Soil Dynamics and Earthquake Engineering*, *159*. https://doi.org/10.1016/j.soildyn.2022.107346

Luo, Y., Fan, X., Huang, R., Wang, Y., Yunus, A. P., & Havenith, H. B. (2020). Topographic and near-surface stratigraphic amplification of the seismic response of a mountain slope revealed by field monitoring and numerical simulations. *Engineering Geology*, *271*. https://doi.org/10.1016/j.enggeo.2020.105607

Massa, M., Lovati, S., D'Alema, E., Ferretti, G., & Bakavoli, M. (2010). An Experimental Approach for Estimating Seismic Amplification Effects at the Top of a Ridge, and the Implication for Ground-Motion Predictions: The Case of Narni, Central Italy. *Bulletin of the Seismological Society of America*, *100*(6), 3020-3034. https://doi.org/10.1785/0120090382

Maufroy, E., Cruz-Atienza, V. M., Cotton, F., & Gaffet, S. (2015). Frequency-Scaled Curvature as a Proxy for Topographic Site-Effect Amplification and Ground-Motion Variability. *Bulletin of the Seismological Society of America*, *105*(1), 354-367. https://doi.org/10.1785/0120140089

Mohammadi, K., & Asimaki, D. (2017). Topography Effects Are Not Dominated by Ground Surface Geometry: A Site Effects Paradox. In *Geotechnical Frontiers 2017* (pp. 171-181). https://doi.org/doi:10.1061/9780784480489.018

Nishimura, K., & Morii, W. (1984). An Observed Effect of Topography on Seismic Ground Motions. *Bulletin of the Disaster Prevention Research Institute*, *34*(4), 203-214. https://doi.org/http://hdl.handle.net/2433/124928

Paolucci, R. (2002). Amplification of earthquake ground motion by steep topographic irregularities. *Earthquake Engineering & Structural Dynamics*, *31*(10), 1831-1853. https://doi.org/10.1002/eqe.192

Park, H.-J., Lee, H., & Kim, B. (2022). Correction factors for GMMs considering site and topographic effects in South Korea. *Bulletin of Earthquake Engineering*, *20*(1), 143-165. https://doi.org/10.1007/s10518-021-01229-3

Perez, V. (1973). Velocity response envelope spectrum as a function of time, for the Pacoima Dam, San Fernando earthquake, February 9, 1971. *Bulletin of the Seismological Society of America*, *63*(1), 299-313. https://doi.org/10.1785/bssa0630010299

Rai, M., Rodriguez-Marek, A., & Chiou, B. S. (2017). Empirical Terrain-Based Topographic Modification Factors for Use in Ground Motion Prediction. *Earthquake Spectra*, *33*(1), 157-177. https://doi.org/10.1193/071015eqs111m

Rai, M., Rodriguez-Marek, A., & Yong, A. (2016). An Empirical Model to Predict Topographic Effects in Strong Ground Motion Using California Small- to Medium-Magnitude Earthquake Database. *Earthquake Spectra*, *32*(2), 1033-1054.

https://doi.org/10.1193/113014eqs202m

Satoh, T., Hayakawa, T., Oshima, M., Kawase, H., Matsushima, S., Nagashima, F., & Tobita, K. (2014). Site Effects on Large Ground Motions at KiK-net Iwase Station IBRH11 during the 2011 Tohoku Earthquake. *Bulletin of the Seismological Society of America*, *104*(2), 653-668. https://doi.org/10.1785/0120130095

Spudich, P., Hellweg, M., & Lee, W. H. K. (1996). Directional topographic site response at Tarzana observed in aftershocks of the 1994 Northridge, California, earthquake: Implications for mainshock motions. *Bulletin of the Seismological Society of America*, *86*(1B), S193-S208. https://doi.org/10.1785/bssa08601bs193

TABLES

Table 1. Regression coefficients of the topographic term proposed in this study for 12 periods ranging from 0.01 to 2 s.

Period (s)	e_1	e_2	e_3	e_4
0.01	1.92×10^{-1}	-3.57×10^{-3}	-1.60×10^{-1}	1.78×10^{-3}
0.02	1.91×10^{-1}	-3.61×10^{-3}	-1.63×10^{-1}	1.78×10^{-3}
0.03	1.77×10^{-1}	-3.58×10^{-3}	-1.67×10^{-1}	1.75×10^{-3}
0.05	1.41×10^{-1}	-3.60×10^{-3}	-1.55×10^{-1}	1.65×10^{-3}
0.075	1.38×10^{-1}	-4.49×10^{-3}	-9.63×10^{-2}	1.27×10^{-3}
0.1	2.54×10^{-1}	-4.64×10^{-3}	-1.20×10^{-1}	2.43×10^{-3}
0.2	3.39×10^{-1}	-3.59×10^{-3}	-2.39×10^{-1}	1.76×10^{-3}
0.3	2.48×10^{-1}	-3.13×10^{-3}	-4.52×10^{-1}	2.90×10^{-3}
0.5	4.79×10^{-2}	-8.55×10^{-4}	-4.96×10^{-1}	2.83×10^{-3}
0.75	-7.93×10^{-2}	6.44×10^{-4}	-4.62×10^{-1}	2.68×10^{-3}
1	-2.18×10^{-2}	2.70×10^{-4}	-4.55×10^{-1}	2.77×10^{-3}
2	-5.91×10^{-2}	6.92×10^{-4}	-1.88×10^{-1}	1.20×10^{-3}

Table 2. Standard deviations (SD) of residuals after the topographic correction across various spatial scales of h_r and α, computed for high- and low-h_r topographic groups for 12 periods ranging from 0.01 to 2 s.

Period (s)	h_r^{500}			h_r^{1000}			h_r^{1500}		
	α^{DEM}	α^{50}	α^{100}	α^{DEM}	α^{50}	α^{100}	α^{DEM}	α^{50}	α^{100}
0.01	0.661	0.667	0.666	0.603	0.597	0.591	0.616	0.613	0.609
0.02	0.661	0.667	0.667	0.603	0.597	0.591	0.616	0.613	0.609
0.03	0.656	0.662	0.662	0.599	0.594	0.588	0.614	0.611	0.607
0.05	0.686	0.694	0.694	0.611	0.606	0.601	0.620	0.618	0.615
0.075	0.733	0.737	0.736	0.657	0.647	0.640	0.660	0.653	0.649
0.1	0.728	0.731	0.730	0.657	0.646	0.640	0.668	0.661	0.658
0.2	0.741	0.744	0.743	0.688	0.682	0.677	0.703	0.699	0.696
0.3	0.670	0.675	0.675	0.676	0.671	0.666	0.696	0.688	0.683
0.5	0.586	0.593	0.594	0.649	0.649	0.647	0.672	0.670	0.668
0.75	0.578	0.583	0.584	0.623	0.626	0.626	0.637	0.639	0.638
1	0.551	0.558	0.559	0.573	0.578	0.577	0.582	0.587	0.586
2	0.496	0.500	0.500	0.509	0.516	0.518	0.482	0.488	0.489

FIGURES

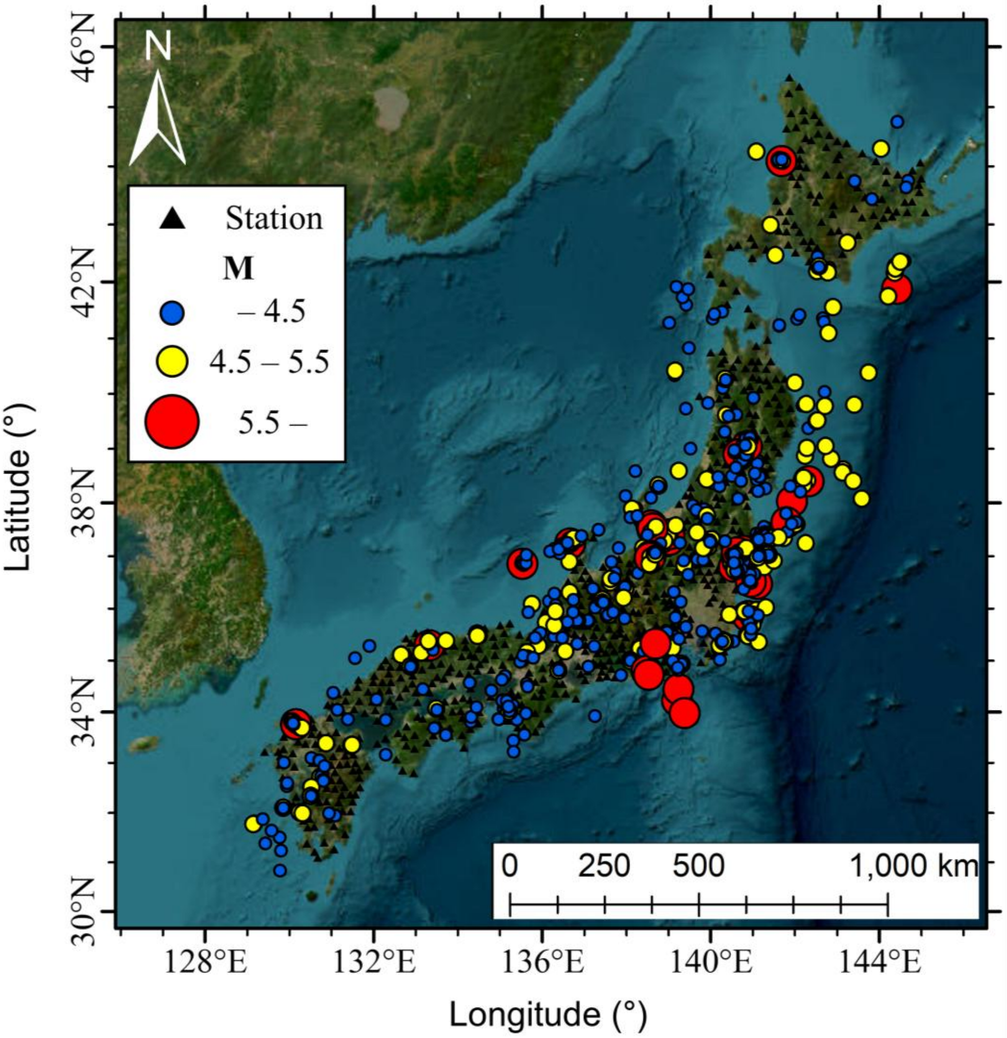

Figure 1. Location of the selected KiK-net stations and earthquakes. Color and size of markers denote moment magnitude.

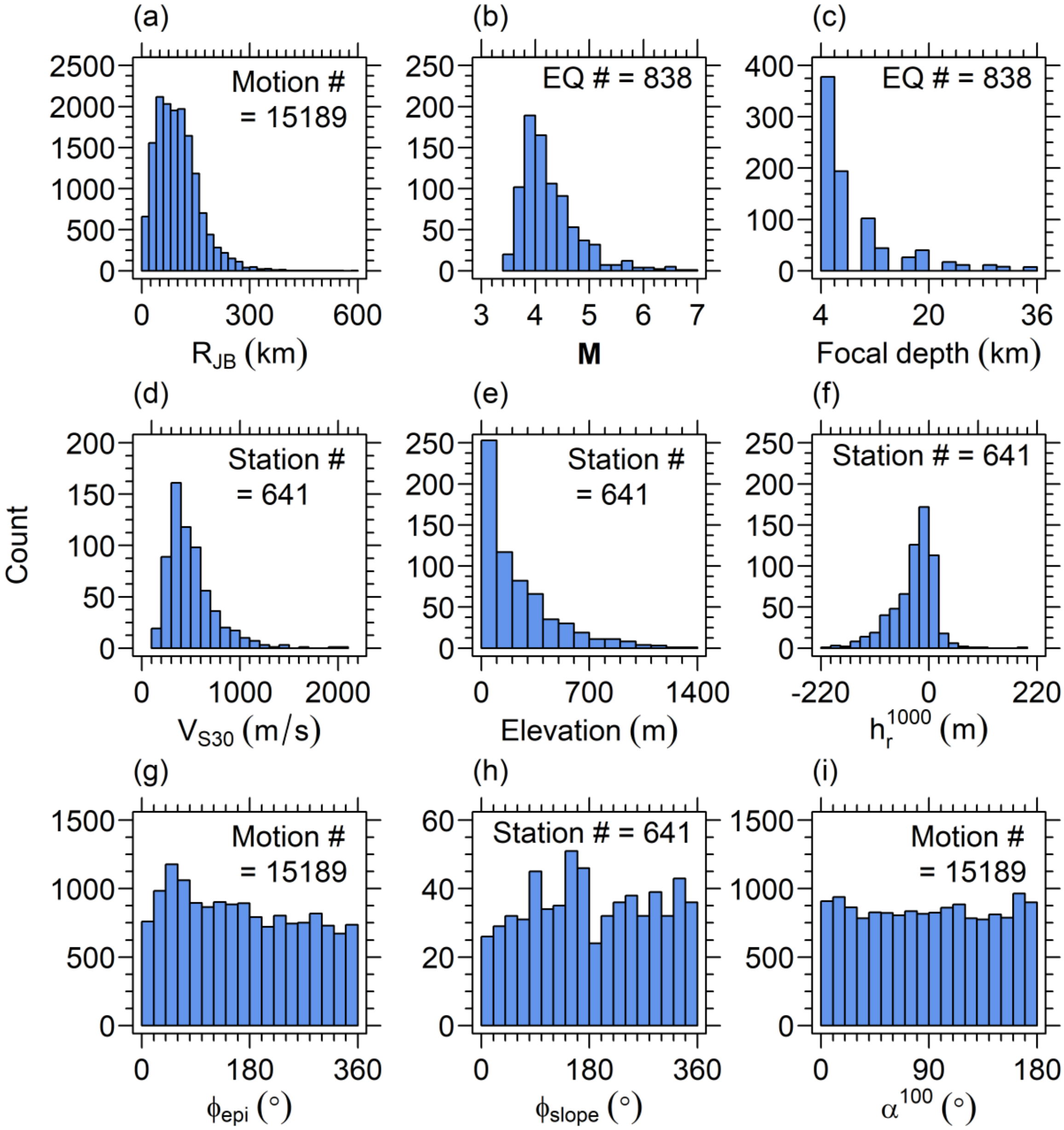

Figure 2. The data distributions of (a) the Joyner–Boore distance (R_{JB}), (b) moment magnitude, (c) focal depth, (d) V_{S30}, (e) elevation, (f) h_r^{1000}, (g) ϕ_{epi}, (h) ϕ_{slope}, and (i) α^{100}.

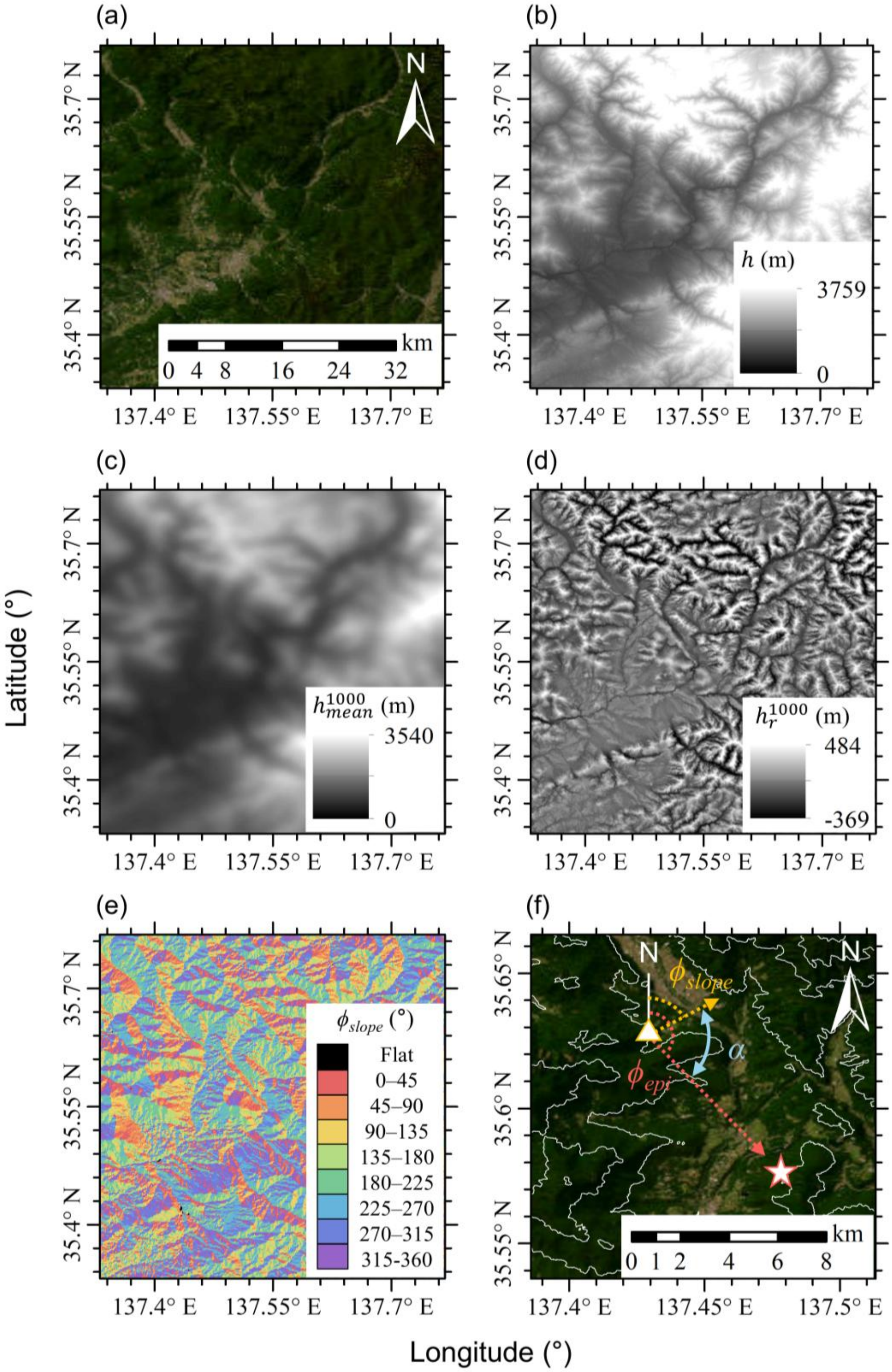

Figure 3. Maps of (a) satellite image, (b) digital elevation model (DEM), (c) mean elevation within 1000 m, (d) the relative elevation at a 1,000 m-scale, (e) ϕ_{slope}, and (f) an example of α.

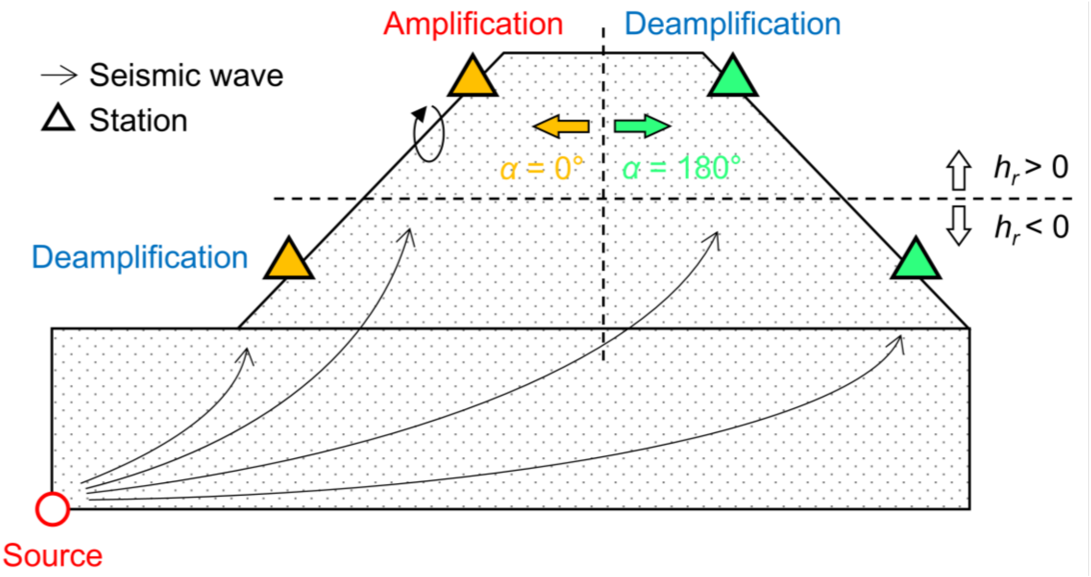

Figure 4. Conceptual schematic illustrating the interaction between terrain geometry (h_r) and seismic incidence direction (α) on ground motion response. The diagram identifies four distinct topographic configurations based on h_r and α.

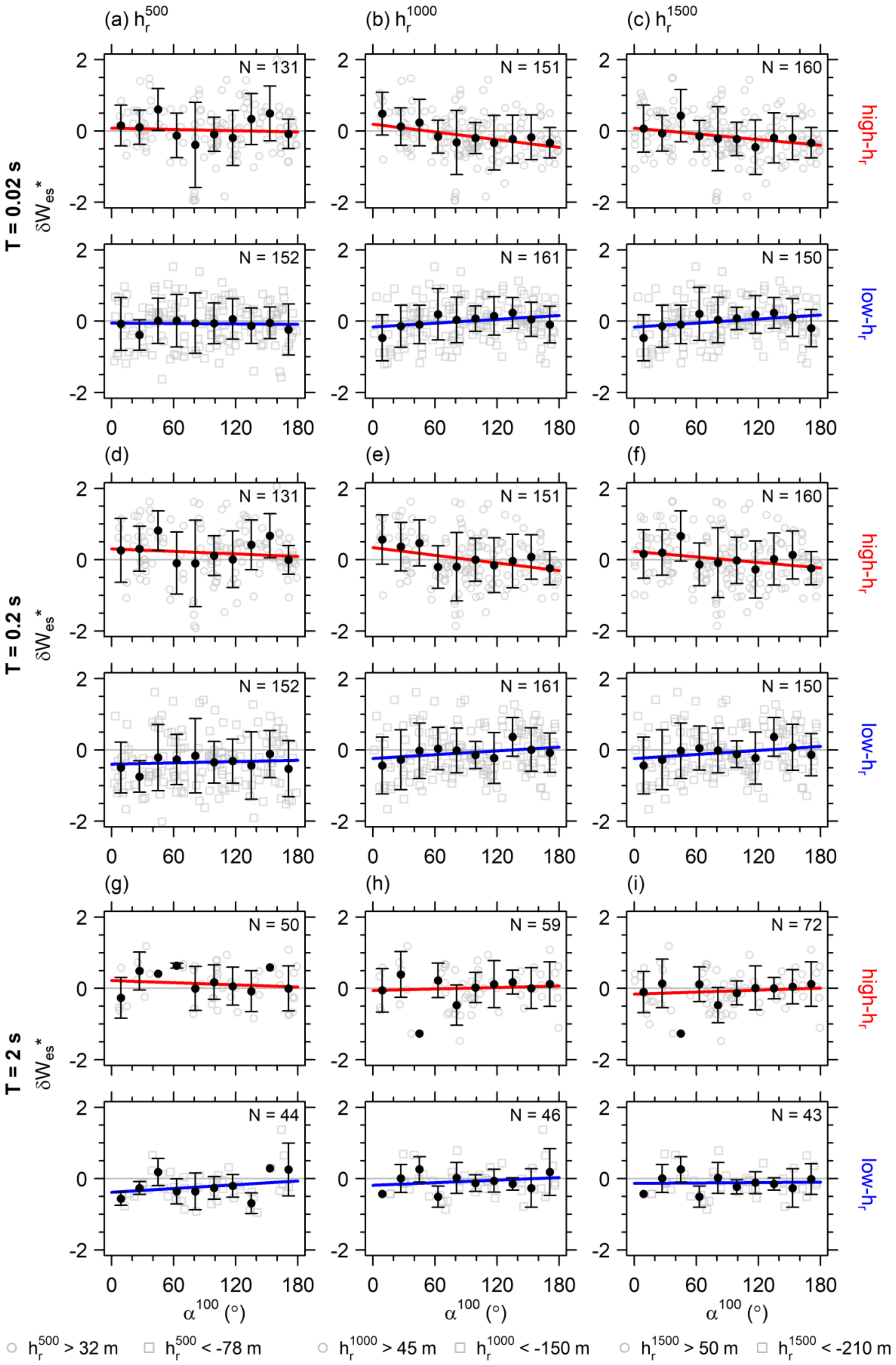

(a) h_r^{500}
(b) h_r^{1000}
(c) h_r^{1500}
(d)
(e)
(f)
(g)
(h)
(i)
T = 0.02 s
T = 0.2 s
T = 2 s
δW_{es}^*
N = 131
N = 151
N = 160
N = 152
N = 161
N = 150
N = 131
N = 151
N = 160
N = 152
N = 161
N = 150
N = 50
N = 59
N = 72
N = 44
N = 46
N = 43
high-h_r
low-h_r
2
0
-2
0
60
120
180
α^{100} (°)
○ h_r^{500} > 32 m
□ h_r^{500} < -78 m
○ h_r^{1000} > 45 m
□ h_r^{1000} < -150 m
○ h_r^{1500} > 50 m
□ h_r^{1500} < -210 m

Figure 5. The V_{S30} scaled within-event residual (δW_{es}^{*}) against the smoothed α at a 100 m-scale (α^{100}). Rows and columns correspond to spectral periods (0.02, 0.2, and 2 s) and radii of the relative elevation, respectively. High-(gray circles, red lines) and low-h_r groups (gray squares, blue lines) are shown with their corresponding fits. Error bars denote grouped mean ± one standard deviation.

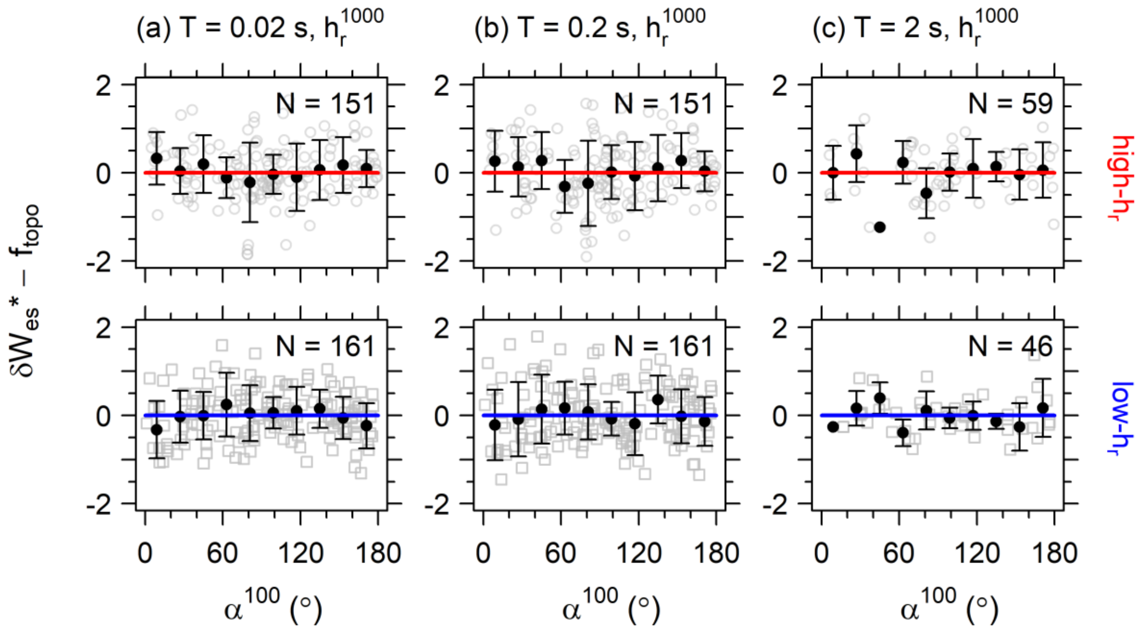

Figure 6. Topography-corrected residuals against α^{100}. Gray circles and squares denote high- and low-h_r for a 1000 m-scale, respectively. Error bars represent grouped mean ± one standard deviation.

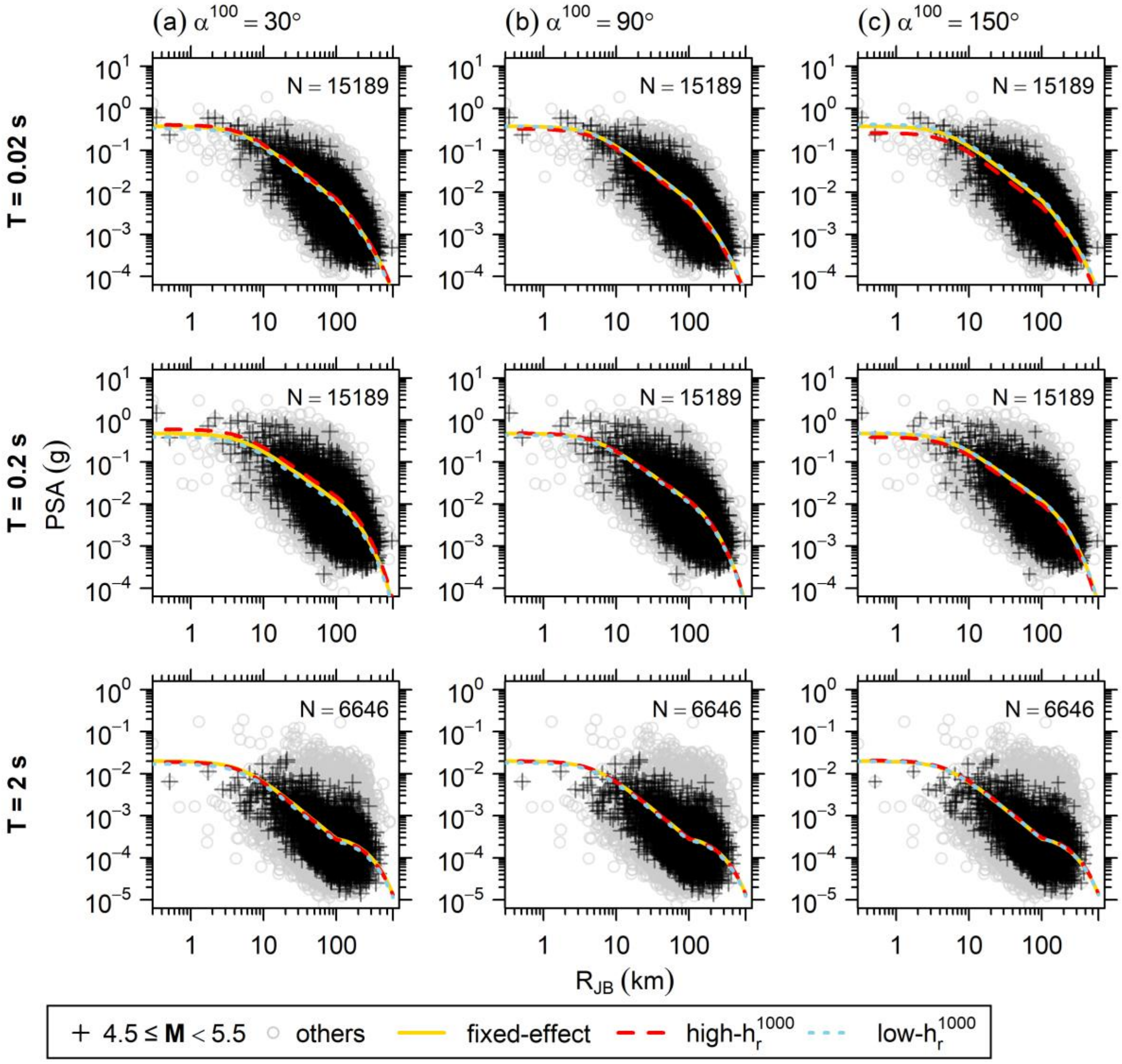

Figure 7. Measured geometric-mean horizontal PSA versus R_{JB} at T = 0.02, 0.2, and 2 s across variations in α^{100}: (a) 30°, (b) 90°, and (c) 150°. Black crosses denote events with magnitudes between 4.5 and 5.5, while gray circles denote all other events. The predictions are conditioned on a fixed magnitude (**M** 5.0). Yellow solid lines denote the predictions from the base model including f_R and f_M. Red dashed lines and blue dotted lines represent the predictions from the proposed GMM incorporating f_R, f_M, and f_{topo}.

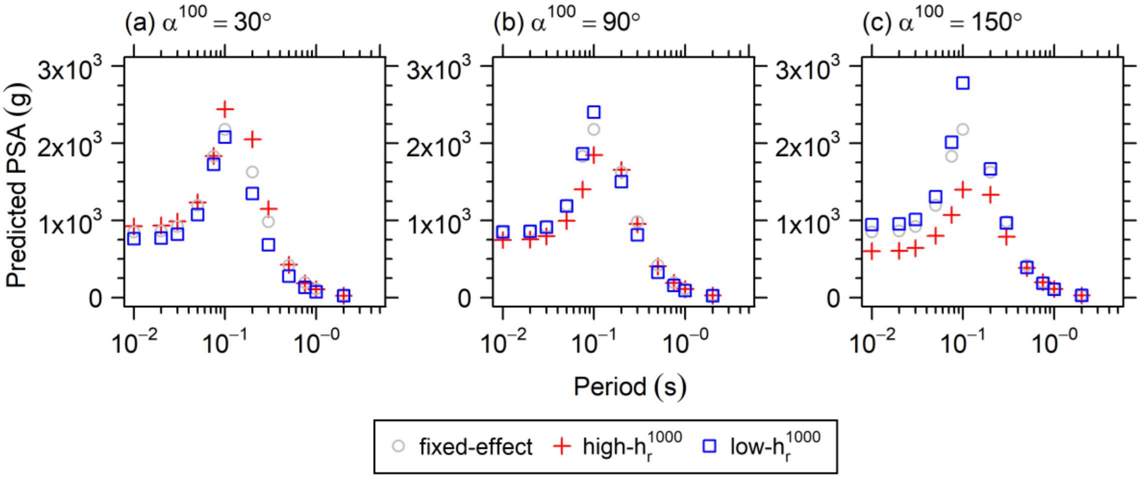

Figure 8. Predicted geometric-mean horizontal PSA from the base and proposed GMMs versus various periods across variations in α^{100}: (a) 30°, (b) 90°, and (c) 150°. The predictions are conditioned on a fixed magnitude (**M** 4.0) and source-to-site distance (R_{JB} = 150 km). Gray circles denote the predictions from the base model including f_R and f_M. Red crosses and blue squares represent the predictions from the proposed GMM incorporating f_R, f_M, and f_{topo}.

APPENDIX

The specific functional forms for f_{R} and f_{M} were adapted from Ko18, as follows:

$$f_{\mathrm{R}}(\mathbf{M}, R_{JB}) = \begin{cases} c_1 \ln\sqrt{R_{JB}^2 + h^2} & R_{JB} < 100 \text{ km} \\ c_1 \ln\sqrt{100^2 + h^2} + c_2 \ln\left(\frac{R_{JB}}{100}\right) + c_3\left(R_{JB} - 100\right) & R_{JB} \geq 100 \text{ km} \end{cases} \quad \text{(A1)}$$

$$\ln(h) = 2.303(\max[(-0.05 + 0.15\mathbf{M}), (-1.72 + 0.43\mathbf{M})]) \quad \text{(A2)}$$

$$f_{\mathrm{M}}(\mathbf{M}) = \begin{cases} a + b_1(\mathbf{M} - \mathrm{M_{ref}}) & \mathbf{M} < \mathrm{M_{ref}} \\ a + b_2(\mathbf{M} - \mathrm{M_{ref}}) & \mathrm{M_{ref}} \leq \mathbf{M} < \mathrm{M_h} \\ a + b_2(\mathrm{M_h} - \mathrm{M_{ref}}) + b_3(\mathbf{M} - \mathrm{M_h}) & \mathrm{M_h} \leq \mathbf{M} \end{cases} \quad \text{(A3)}$$

where c_1, c_2, c_3, a, b_1, b_2, and b_3 are regression coefficients. The reference magnitude ($\mathrm{M_{ref}}$) is set to 4.5, while the period-dependent hinge magnitude ($\mathrm{M_h}$) is fixed at 5.5 for spectral periods up to 0.1 s and increases linearly with the logarithmic period for those exceeding 0.1 s, as described in Ko18. Although the functional forms follow Ko18, all regression coefficients (c_1, c_2, c_3, a, b_1, b_2, b_3) were calibrated through a regression analysis using our dataset. The regression coefficients for f_{R} and f_{M} are listed in

Table A1.

As illustrated in Figure A1, between-event residuals and within-event residuals exhibit no systematic trends with respect to **M** and R_{JB}, respectively.

Figure A2 illustrates the relationship between station-averaged within-event residuals and V_{S30} for each spectral period. A LOESS regression was applied to the data to capture the V_{S30}-dependent site effects, which was subsequently used to correct the within-event residuals.

Figure A3 shows δWes* versus α^{100} for the intermediate-h_r groups identified using h_r^{500}, h_r^{1000}, and h_r^{1500}. As illustrated in Figure A3, these intermediate groups do not exhibit any apparent azimuthal dependence, maintaining a residual trend close to zero regardless of α^{100} across the h_r scales.

Table A1. Regression coefficients for the reference ground motion model (GMM) covering the distance and magnitude scaling terms. These coefficients are derived from following the parametric regression form by Kotha et al. (2018).

Period (s)	c_1	c_2	c_3	a	b_1	b_2	b_3
0.01	-1.355	-1.353	-0.0053	0.486	0.999	1.402	0.900
0.02	-1.354	-1.388	-0.0052	0.497	0.995	1.398	0.902
0.03	-1.350	-1.609	-0.0042	0.572	0.968	1.379	0.894
0.05	-1.316	-2.164	-0.0021	0.756	0.893	1.313	0.864
0.075	-1.239	-2.282	-0.0022	0.877	0.879	1.263	0.837
0.1	-1.216	-1.797	-0.0046	0.893	0.929	1.294	0.852
0.2	-1.233	-0.421	-0.0098	0.516	1.194	1.462	0.782
0.3	-1.298	0.228	-0.0118	0.267	1.438	1.557	0.752
0.5	-1.373	0.894	-0.0137	-0.246	1.787	1.736	0.619
0.75	-1.385	1.028	-0.0132	-0.923	1.993	1.880	0.431
1	-1.340	0.973	-0.0121	-1.689	2.113	2.022	0.200
2	-1.419	0.503	-0.0079	-2.757	2.141	2.241	-0.149

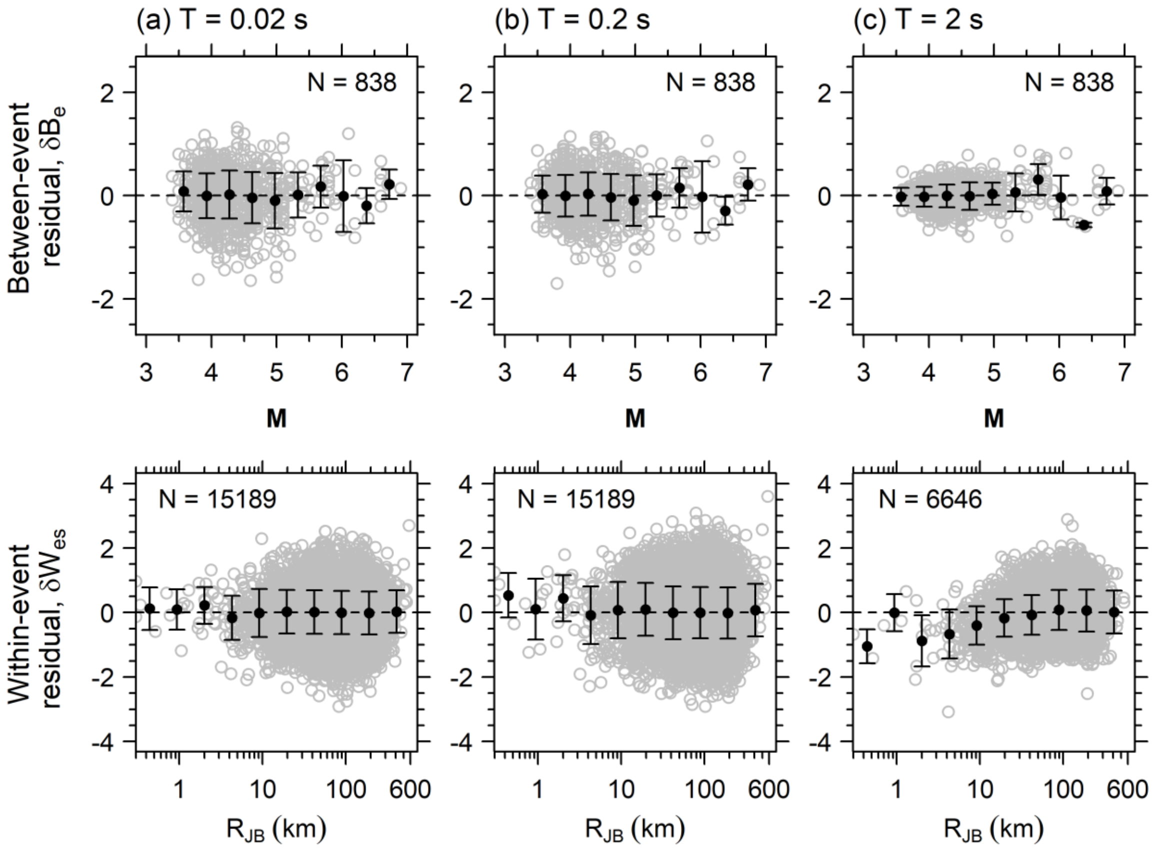

Figure A1. Between-event residuals versus **M** and within-event residuals versus R_{JB}. The black circles and error bars represent grouped mean ± one standard deviation.

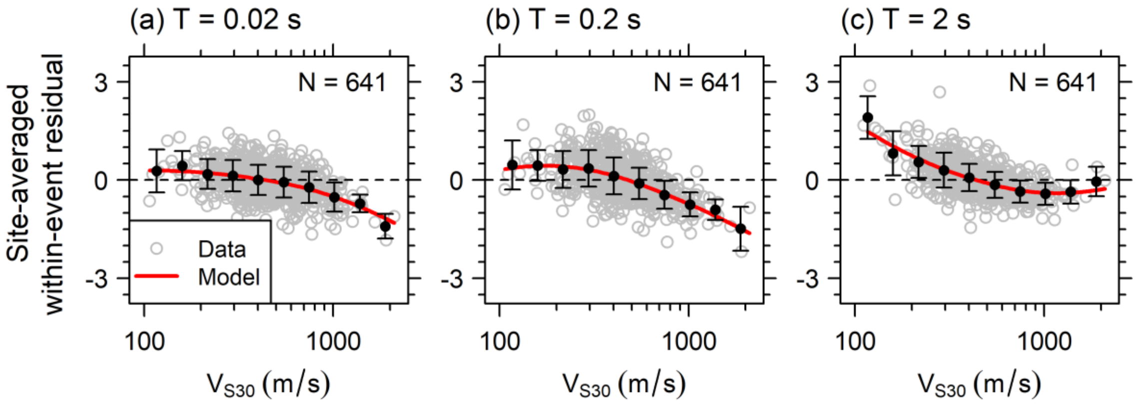

Figure A2. Site-averaged within-event residual versus V_{S30}. The red solid line represents the LOESS regression fit and black circles with error bars represent grouped mean ± one standard deviation.

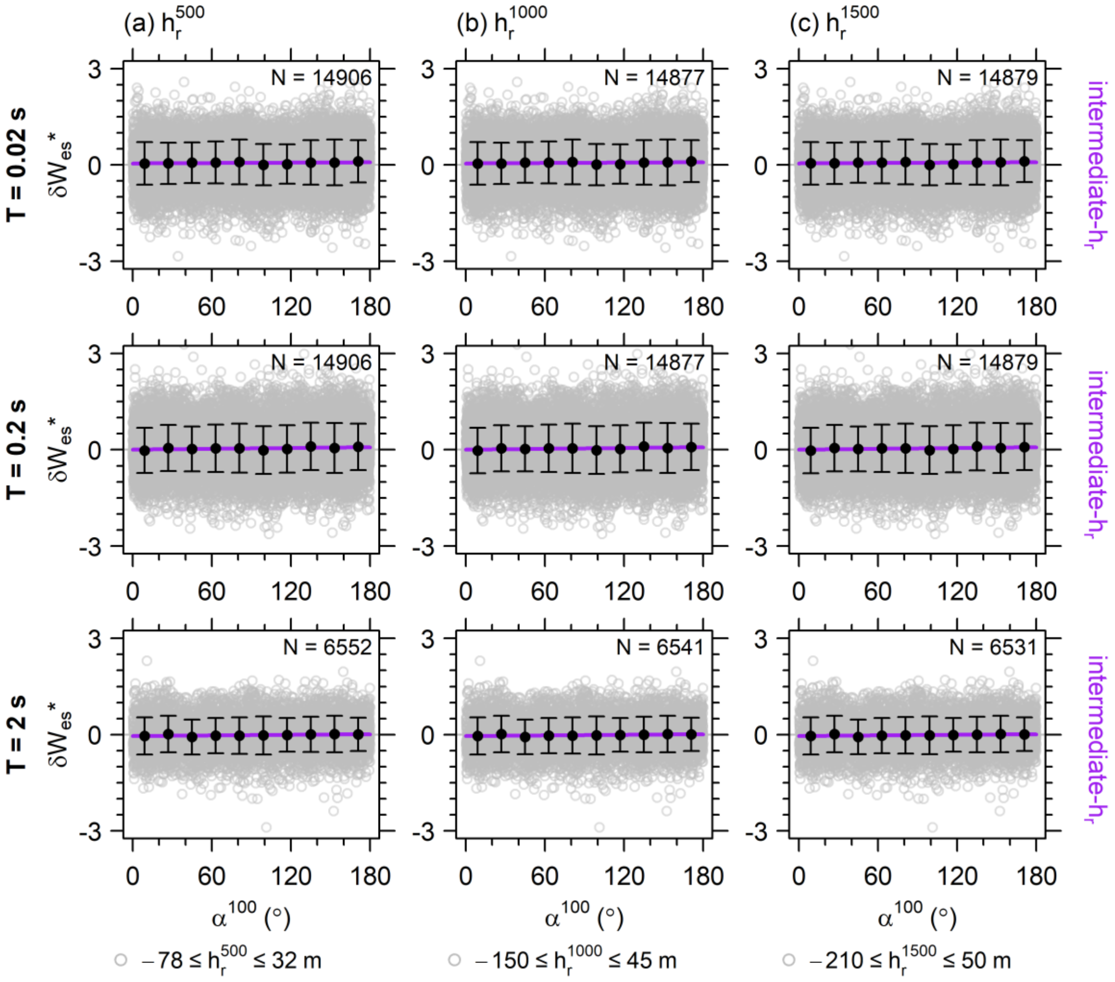

Figure A3. The V_{S30} scaled within-event residual (δW_{es}^*) against the smoothed α at a 100 m-scale (α^{100}). Rows and columns correspond to spectral periods (0.02, 0.2, and 2 s) and radii of the relative elevation, respectively. Intermediate-h_r groups (gray circles) are shown with its corresponding fits (purple lines). Error bars denote grouped mean ± one standard deviation.